



# Nanosheets based mesoporous NiO microspherical structures via facile and template-free method for high performance supercapacitors

Jeong Woo Lee<sup>a</sup>, Taebin Ahn<sup>a</sup>, Jong Hun Kim<sup>a</sup>, Jang Myoun Ko<sup>b</sup>, Jong-Duk Kim<sup>a,\*</sup>

<sup>a</sup> Department of Chemical and Biomolecular Engineering, Center for Energy and Environment Engineering, Korea Advanced Institute of Science and Technology (KAIST), 373-1, Guseong-dong, Yuseong-gu, Daejeon, P. O. 305-701, Republic of Korea

<sup>b</sup> Department of Applied Chemistry and Biotechnology, Hanbat National University, San 16-1, Dukmyung-dong, Yuseong-gu, Daejeon, P. O. 305-719, Republic of Korea

## ARTICLE INFO

### Article history:

Received 1 November 2010

Received in revised form 7 January 2011

Accepted 23 February 2011

Available online 6 March 2011

### Keywords:

NiO

Supercapacitor

## ABSTRACT

A novel template-free method to synthesize NiO microstructures is reported and the electrochemical properties of the fabricated microstructures are evaluated. Applying hexamethylenetetramine hydrolysis under a refluxing condition for 2 h,  $\alpha$ -Ni(OH)<sub>2</sub> microstructures were synthesized, subsequent calcination at 300 °C yielded NiO microstructures that retained the morphologies of their predecessors. The fabricated NiO microstructures had high specific surface area, large pore volume, and narrow pore size distribution making them ideal candidates for supercapacitor applications. The NiO microstructures have the high specific capacitance and displayed a good retention for more than 1000 cycles in a cycling test. The results suggest that NiO microstructures are a promising supercapacitor electrode material.

© 2011 Elsevier Ltd. All rights reserved.

## 1. Introduction

Supercapacitors, also known as electrochemical capacitors or ultracapacitors have garnered considerable attention over the past decade due to their high power density and longer cycle ability compared to secondary batteries and conventional dielectric capacitors [1,2]. Many studies have accordingly been carried out during in the past few years in effort to improve the performance of electrochemical capacitor electrodes and to develop replacements for batteries. Supercapacitors are generally classified into two types, electrical double layer capacitors (EDLCs) and pseudocapacitors, depending upon the charge storage mechanism. EDLCs function on the basis of charge the separation at electrode and an electrolyte interface. The most commonly used materials for EDLCs are activated carbons [3,4]. Pseudocapacitors, meanwhile, are based on a fast, reversible redox process occurring at or near the active electrode surface [5,6]. Among the pseudocapacitors, various types of ruthenium oxides with high capacitance have been extensively studied for active electrode applications [7–10]. However, they are limited to commercial products due to their costliness and toxic nature. Hence, many efforts have been exerted to replace RuO<sub>2</sub> by other transition metal oxide such as NiO [11–15], Co<sub>3</sub>O<sub>4</sub> [16], MnO<sub>2</sub> [17], SnO<sub>2</sub> [18], Fe<sub>3</sub>O<sub>4</sub> [19], etc.

Among transition metal oxides, NiO has been widely studied due to its high surface area, high specific capacitance, and low cost. Furthermore, the theoretical specific capacitance of NiO is

2584 Fg<sup>-1</sup> within 0.5 V [20], suggesting its potential application as an electrochemical material. In general, the specific capacitance of pseudocapacitors arises from the interface of the electrode. Therefore, it is desirable to produce electrode materials with high specific surface area as well as suitable pore size distribution. High specific surface area induces the formation of many electrical double layers and employs more electroactive species in pseudocapacitive reactions. Appropriate narrow pore size distribution (2–5 nm) helps the mass transfer of electrolytes within the pores for fast redox reactions and double layer charging/discharging reaction [11,12,14]. Thus, most studies have aimed at enhancing the electrochemical properties of NiO.

To date, various routes to fabricate NiO electrodes have been reported including film-type using electrodeposition methods [21–23] and chemical bath deposition [24]. Powder-type electrodes have also been produced, using a soft or hard template, [12–14] hydrothermal processes [12,25], and precipitation methods [12–14,26–31]. NiO film can be obtained by tuning deposition parameters, but the product mass is quite small, thus limiting large-scale production of electrode materials. In the case of the template method, additional cost is incurred and complex procedures are needed to remove the template. The hydrothermal method is effective in terms of controlling the morphology and size of products. However, the hydrothermal process in an autoclave limits fine control over reactions and large-scale production.

Precipitation methods are simple as well as effective to obtain desired products. Depending on the method of supplying of OH<sup>-</sup>, the precipitation method generally can be classified into two-types: (i) coprecipitation methods, which generally control pH of a solution containing precursors, where NH<sub>4</sub>OH [15,26–28], KOH [29],

\* Corresponding author. Tel.: +82 042 350 3921; fax: +82 042 350 3910.  
E-mail address: [jdkim@kaist.ac.kr](mailto:jdkim@kaist.ac.kr) (J.-D. Kim).

NaOH [30], and LiOH [31] are used as alkaline sources to produce the OH<sup>-</sup> group; (ii) homogeneous precipitation methods, where the solution is rendered to have a basic condition, preventing sudden change of the pH by slow and progressive hydrolysis, where urea [13,14,25] and hexamethylenetetramine (HMT) are widely used as hydrolysis agents.

In this article, we report on the template-free synthesis of NiO spherical microstructures by HMT hydrolysis employing a refluxing condition for 2 h without any template agents or seed. To the best of our knowledge, this is the first report of powder-type NiO electrodes synthesized by HMT hydrolysis. The fabricated NiO microstructures have high specific surface area, large pore volume area, and narrow pore size distribution, constituting ideal supercapacitive properties, thus suggesting that HMT is an effective alkaline source to fabricate NiO electrodes. From the results of electrochemical experiments, the NiO microstructures show specific capacitance of 403 Fg<sup>-1</sup> at 20 mV s<sup>-1</sup> and good retention after 1000 cycles in a cycling test. Based on this high specific capacitance and electrochemical stability, they hold promise for application as supercapacitor electrode.

## 2. Experimental

### 2.1. Preparation of NiO microstructures

Nickel sulfate (NiSO<sub>4</sub>·6H<sub>2</sub>O) and hexamethylenetetramine (HMT, C<sub>6</sub>H<sub>12</sub>N<sub>4</sub>) were purchased from Sigma–Aldrich. All reagents were used as received without any further purification. Deionized water was used throughout the experiment. A mixture of NiSO<sub>4</sub>·6H<sub>2</sub>O (0.01 mol) and HMT (0.1 mol) was dissolved in 400 mL of water, and the solution was heated at refluxing temperature under continuous magnetic stirring. The refluxing period was set at 2 h. After the reaction, the solution was cooled naturally to room temperature. The green precipitate was separated, washed with water several times, and dried overnight at room temperature under a vacuum condition. NiO microstructures were obtained by calcination of green powder in air at 300, 400, and 500 °C for 3 h, which are denoted as N300, N400, and N500, respectively.

### 2.2. Sample characterization

The crystal structures were analyzed by X-ray diffraction (XRD, Rigaku D/MAX–IIIC) equipped with Cu–Kα radiation (λ = 1.50405 Å). To investigate the morphology of the structures, field emission scanning electron microscopy (FE–SEM) images were obtained by using a Nova 230 (FEI Company). Transmission electron microscopy (TEM) images and selected electron diffraction (SAED) pattern were taken on a JEM–2100F at 200 kV. A Thermogravimetry analysis (TGA) was performed at a heating rate of 10 °C min<sup>-1</sup> in air on a thermal analyzer (NETSCH TG 209 F3, Germany). The specific surface area, total pore volumes, and pore size distribution were obtained from a N<sub>2</sub> adsorption/desorption analysis conducted at 77 K on a Micromeritics Tristar II 3020 system. The specific surface area was calculated by the Brunauer–Emmett–Teller (BET) method, and pore size distribution was obtained from a desorption plot by a Barrett–Joyner–Halenda (BJH) analysis.

### 2.3. Electrode preparation

To evaluate the electrochemical properties of the NiO microstructures, working electrodes were prepared as follows. The prepared NiO microstructures, vapor grown carbon fiber (VGCF, Showa Denko K.K., Japan, specific area: 13 m<sup>2</sup> g<sup>-1</sup>, aspect ratio: 67) as a conducting material and polyvinylidene fluoride (PVDF) as a binder, respectively, were mixed in a weight ratio of 80:10:10 to yield a paste. N-methyl-2-pyrrolidone (NMP) was used as a

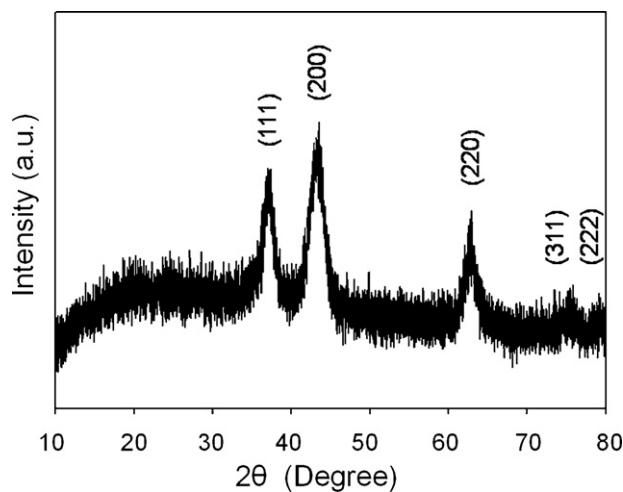


Fig. 1. XRD pattern of NiO microstructures.

solvent. The obtained paste was incorporated into nickel foam (1 cm × 1 cm). The mass of active materials in working electrode was 0.8 mg. Prepared working electrodes were dried at room temperature for 1 day, and then under vacuum at room temperature overnight. Dried working electrodes were pressed, and its thickness was 0.7 mm.

### 2.4. Electrochemical measurements

Electrochemical studies were carried out by measurement of cyclic voltammetry (CV) and impedance of half cells using AUTOLAB (ECO CHEMIE, PGSTAT 100). A beaker type three-electrode cell equipped with a NiO microstructures current collector on nickel foam as a working electrode, an Ag/AgCl electrode (Metrohm AG 9101 Herisau, 3 M KCl, 0.222 V vs. SHE at 25 °C) as a reference electrode, and a Pt plate (2 cm × 2 cm) as a counter electrode was used. A Luggin capillary tip was kept as close as 1–2 mm to the working electrode, and was set to minimize error due to *iR* drop in the electrolyte. Electrochemical impedance measurements were conducted for the working electrode in a frequency range of 100 kHz to 0.01 Hz with ac perturbation of 5 mV. For all electrochemical characterizations, a test solution of 6 M KOH was used as an electrolyte solution. The specific capacitance was calculated from the cyclic voltammetry (CV) curves based on the following equation [32,33]:

$$C = \frac{q_a + q_c}{2m\Delta V} \quad (1)$$

where  $q_a$ ,  $q_c$ ,  $m$ , and  $\Delta V$  are the sums of anodic and cathodic voltammetric charges on the anodic and cathodic scans, the mass of the active material and potential window of cyclic voltammetry, respectively.

## 3. Results and discussion

### 3.1. Characterization of NiO microstructures

The XRD pattern of black powder obtained after the calcination process is shown in Fig. 1. The diffraction peaks are indexed at  $2\theta = 37.2^\circ$ ,  $43.2^\circ$ ,  $62.8^\circ$ ,  $75.4^\circ$ , and  $79.4^\circ$ , which correspond to the (1 1 0), (2 0 0), (2 2 0), (3 1 1), and (2 2 2) reflections of NiO structures (JCPDS card no. 47–1049). A temperature of 300 °C was sufficient to drive to the conversion to NiO, and no peaks of impurities were observed.

To investigate the morphologies of the obtained NiO, SEM measurement was performed, and SEM images of NiO are shown in Fig. 2. Spherical-type structures were found over the samples, and

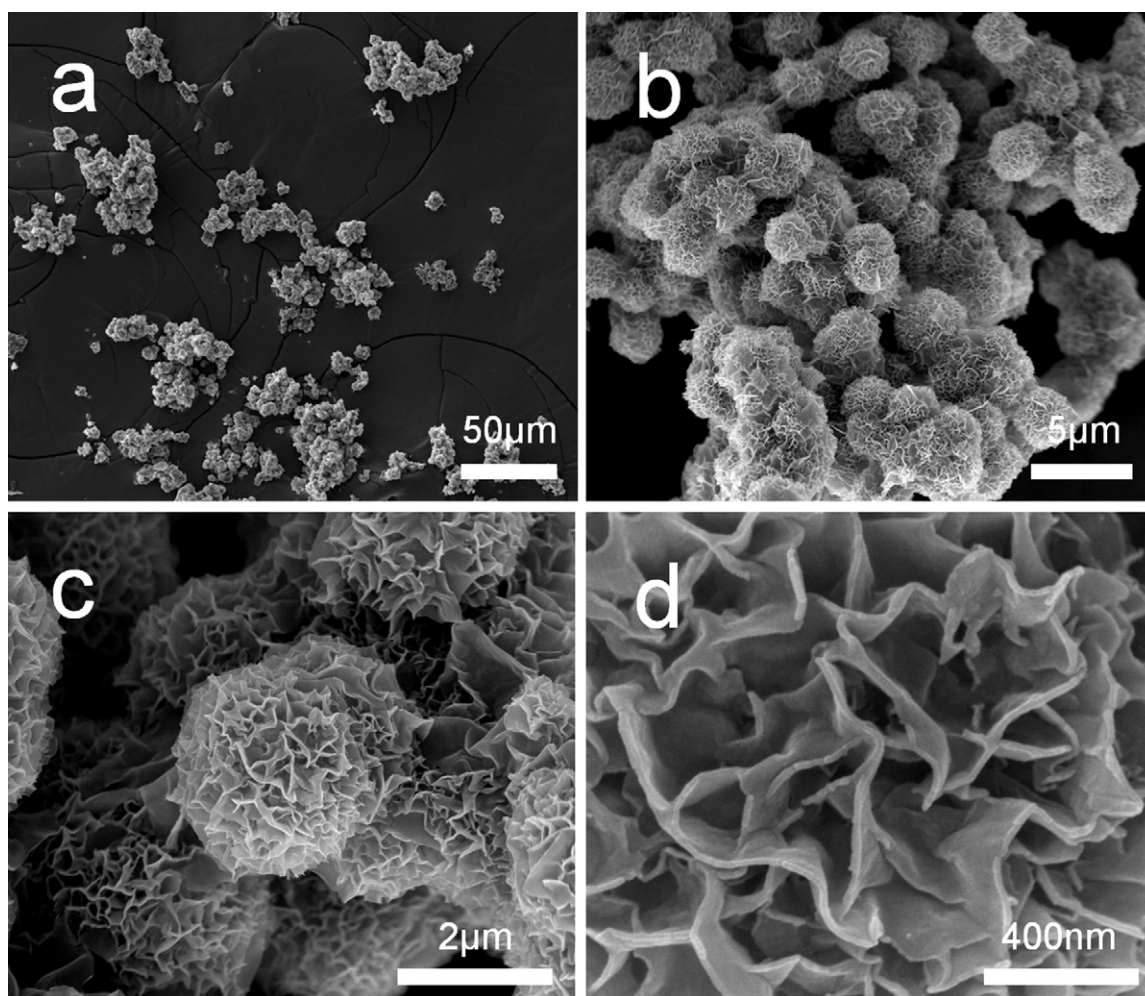


Fig. 2. SEM images of NiO microstructures at different magnifications.

appeared to be massed with each other. At a high magnification (Fig. 2d), thin and highly vented nanosheets were disorderly interconnected in a disorderly arrangement. The estimated thickness of the nanosheets was around 10–30 nm. It was speculated that these unique structures might have high surface area, and consequently, could provide high specific capacitance due to easy access of the active species in the redox process at the interface of the electrode.

To estimate the surface area of NiO microstructures, BET measurements were carried out, and nitrogen adsorption/desorption isotherms of N300, N400, and N500, respectively are shown in Fig. 3a–c. BET surface area and total pore volume of N300, N400, and N500 are shown in Table 1. According to the IUPAC classification, all isotherm can be classified as type IV with H4 type hysteresis behavior. The type IV isotherm is obtained with mesoporous ( $2 \text{ nm} < \text{pore size} < 50 \text{ nm}$ ) materials. Meanwhile, the hysteresis loop is associated with the secondary process of capillary condensation, which starts at about  $P/P_0 = 0.4$  and extends almost to  $P/P_0 = 1$ , suggesting complete filling of the mesopores. This indicates that NiO microstructures are mesoporous materials with a high fraction of textural porosity. The measured BET specific surface area of N300, N400, and N500 were 258.52, 227.13, and 125.39  $\text{m}^2 \text{g}^{-1}$ , respectively, which is higher than those of reported NiO particles [11,13,15]. The pore size distribution of sample N300 (Fig. 3d) is narrow with a single modal centered at 3.8 nm. Such small pores are presumably generated from pore opening when the physical absorbed water or intercalated water were removed between  $\text{Ni}(\text{OH})_2$  layers. At high temperature ( $400^\circ\text{C}$ ), pore size became

larger and broader with a bimodal size distribution at 5.1 and 7.9 nm due to expansion of pores. With further increase in calcination temperature ( $500^\circ\text{C}$ ), the bimodal size distribution became apparent, namely, at 4–6 nm and 7–11 nm. The total pore volumes of N300, N400, and N500 were 0.633, 0.692, and 0.640  $\text{cm}^3 \text{g}^{-1}$ , respectively. As the calcination temperature increased, the specific surface area was dramatically reduced due to collapse or sintering small pore walls. In conclusion, the BJH pore size distribution of N300 is a single modal centered at 3.8 nm, and the NiO microstructures has a uniform framework with both a regular mesopore size distribution and the optimal pore size range of 2–5 nm, applicable for NiO supercapacitor applications [11,12,14].

### 3.2. Characterization of precursor of NiO microstructures

Since most properties such as morphologies and surface area of NiO are related to the NiO precursor, synthesis and characterization about the NiO precursor are necessary. Fig. 4a shows the

**Table 1**  
Surface properties of prepared N300, N400, and N500.

Sample	BET surface area ( $\text{m}^2 \text{g}^{-1}$ )	Total pore volume ( $\text{cm}^3 \text{g}^{-1}$ )
N300 <sup>a</sup>	258.52	0.633
N400 <sup>a</sup>	227.13	0.692
N500 <sup>a</sup>	125.39	0.640

<sup>a</sup> Samples were obtained by calcination temperature for 3 h.

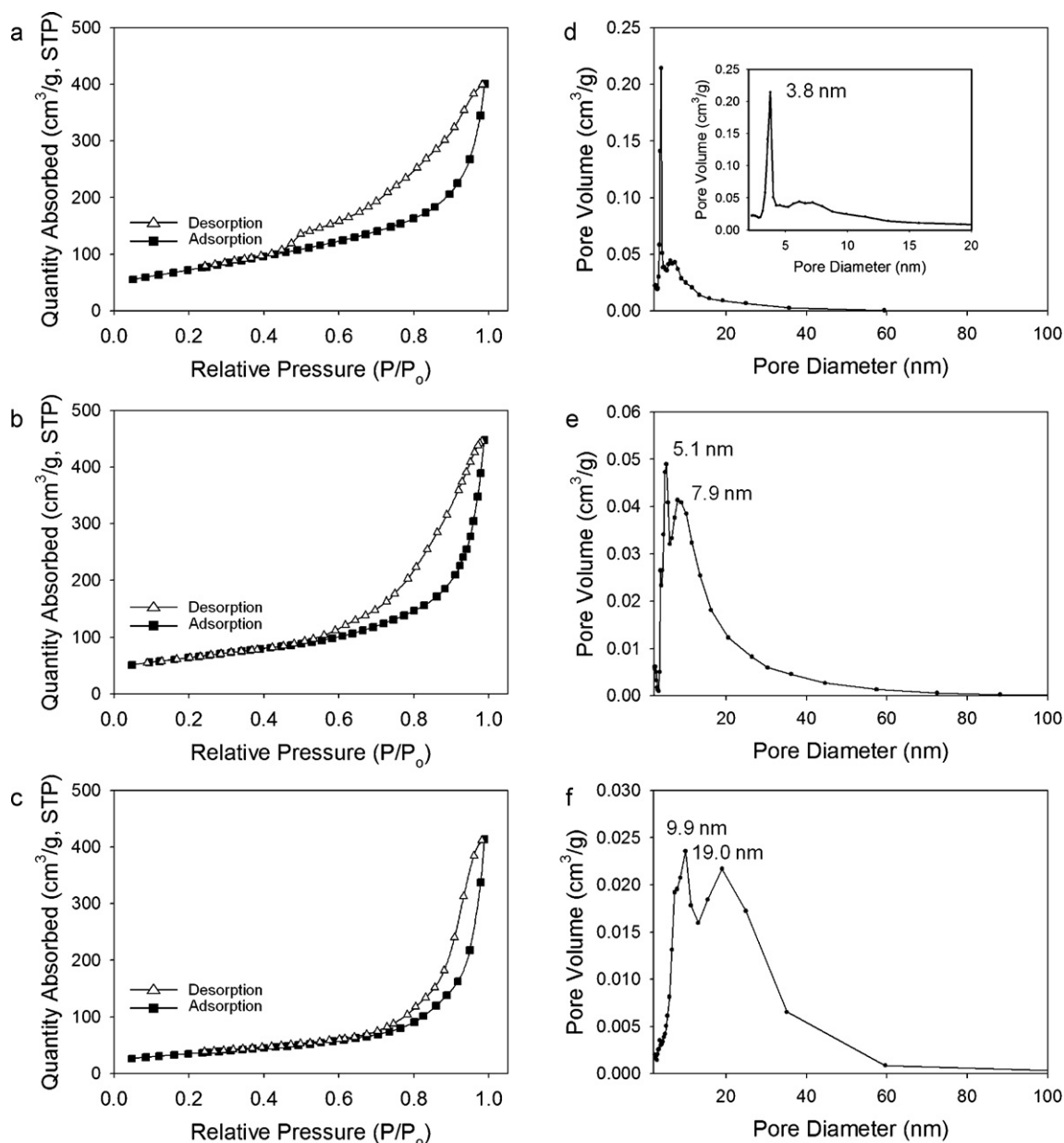


**Fig. 3.** Nitrogen adsorption-desorption isotherms (a)–(c) with corresponding the pore size distributions (d)–(f) of N300 (a) and (d), N400 (b) and (e), and N500 (c) and (f), respectively.

XRD pattern of the green precipitate obtained by HMT hydrolysis. In a low angle range, a diffraction peak around  $10.34^\circ$  was observed, which can be assigned to the (003) plane of  $\alpha$ -Ni(OH)<sub>2</sub> (JCPDS card no. 38-0715). Two broad and asymmetric peaks were observed at about  $33.6^\circ$  and  $60.0^\circ$  corresponding to non-basal spacing, which is present in turbostratic materials. Turbostratic disorder can be explained on the basis of the stacking order of a brucite-like structure parallel and equidistant along the *c*-axis of the hexagonal structure but randomly twisted against each other. This turbostratic behavior has also been observed in other  $\alpha$ -Ni(OH)<sub>2</sub> [34]. During thermal decomposition,  $\alpha$ -Ni(OH)<sub>2</sub> has multistep and larger mass losses compared to  $\beta$ -Ni(OH)<sub>2</sub> (generally 18%), which does not have any anions or water species [34]. TG data (Fig. 4b) shows two-step weight loss at temperatures of around  $60^\circ\text{C}$  and  $300^\circ\text{C}$ . The first-weight loss arose from removal of intercalated water or absorbed water, and the second-weight loss resulted from the decomposition of intercalated anions and dehydration of Ni(OH)<sub>2</sub>.

SEM images of obtained  $\alpha$ -Ni(OH)<sub>2</sub> are shown in Fig. 5a and b, revealing similarity to the NiO microstructure (Fig. 2). This indicates that the pore framework was not destroyed during the calcination process. Fig. 5d shows a selected area electron diffraction (SAED) pattern taken at the nanosheet of  $\alpha$ -Ni(OH)<sub>2</sub>. The SAED displays hexagonally arranged spots as a (*h k 0*) reflection on the (00*l*) plane, which was well matched with the hexagonal  $\alpha$ -Ni(OH)<sub>2</sub> phase. It is thought that hierarchical  $\alpha$ -Ni(OH)<sub>2</sub> consists of numerous thin nanosheets forming a single crystalline state.

### 3.3. Growth mechanism of $\alpha$ -Ni(OH)<sub>2</sub> microstructures

The mechanism underlying the formation of the hierarchically porous morphology was investigated with  $\alpha$ -Ni(OH)<sub>2</sub> collected after reaching the refluxing condition. Fig. 6 shows SEM images of  $\alpha$ -Ni(OH)<sub>2</sub> powder: (a) 5 min and (b) 30 min, respectively. The porous shapes are partially observed on the surface of  $\alpha$ -Ni(OH)<sub>2</sub>

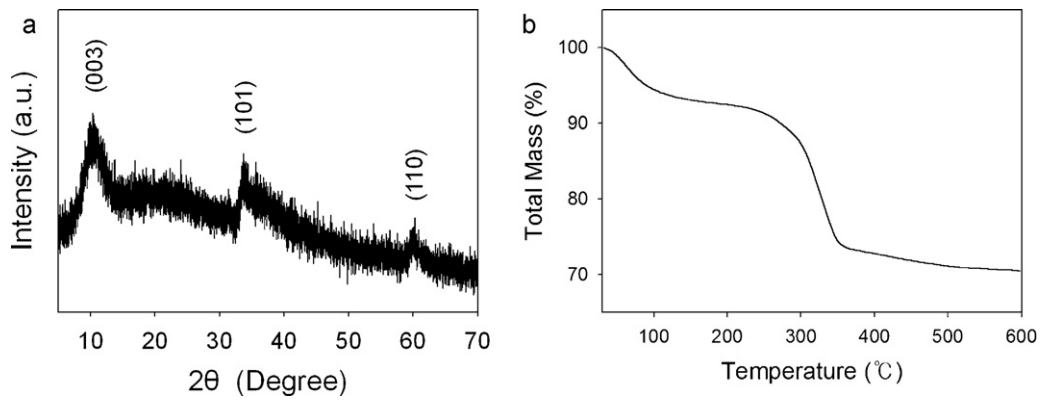


Fig. 4. (a) XRD pattern and (b) TG curve of  $\alpha$ -Ni(OH)<sub>2</sub>.

(Fig. 6a), and as reaction time proceeded, more porous morphologies are observed, as seen in Fig. 6b. On the basis of the evaluation of the time-dependent morphologies, the formation mechanism of porous structures could be attributed to anisotropic Ostwald ripening. At the initial stage of reaction, the precursors tend to dissolve into the solution due to their relatively high surface energy. By supplied energy in the system, the ions are reprecipitated onto the high energy crystallographic facet of the particles, leading to the growth of large particles. Simultaneously, through the attachment and coalescence of particles with favorable crystallographic planes, oriented attachments proceed, resulting in the formation of large aggregated spherical forms. Further growth on the surface of particles progress steadily, forming hierarchically porous mor-

phologies on the surface. This proposed mechanism is supported by SEM images of broken  $\alpha$ -Ni(OH)<sub>2</sub> microstructures obtained after 2 h under a refluxing condition. (Fig. 7) Compared to the porous surface, densely packed regions are observed in the interior. In conclusion, porous  $\alpha$ -Ni(OH)<sub>2</sub> microstructures are thought to result from both Ostwald ripening and oriented attachment. The proposed formation mechanism of  $\alpha$ -Ni(OH)<sub>2</sub> microstructures is illustrated in Fig. 8. Obtained  $\alpha$ -Ni(OH)<sub>2</sub> were transformed to NiO via calcination. Morphologies of NiO microstructures are different from reported other NiO [11,13,14,28,30]. During the calcination, the hierarchical morphologies of NiO did not changed, but maintained the high specific area and narrow pore size distribution observed by BET and BJH results. The large surface

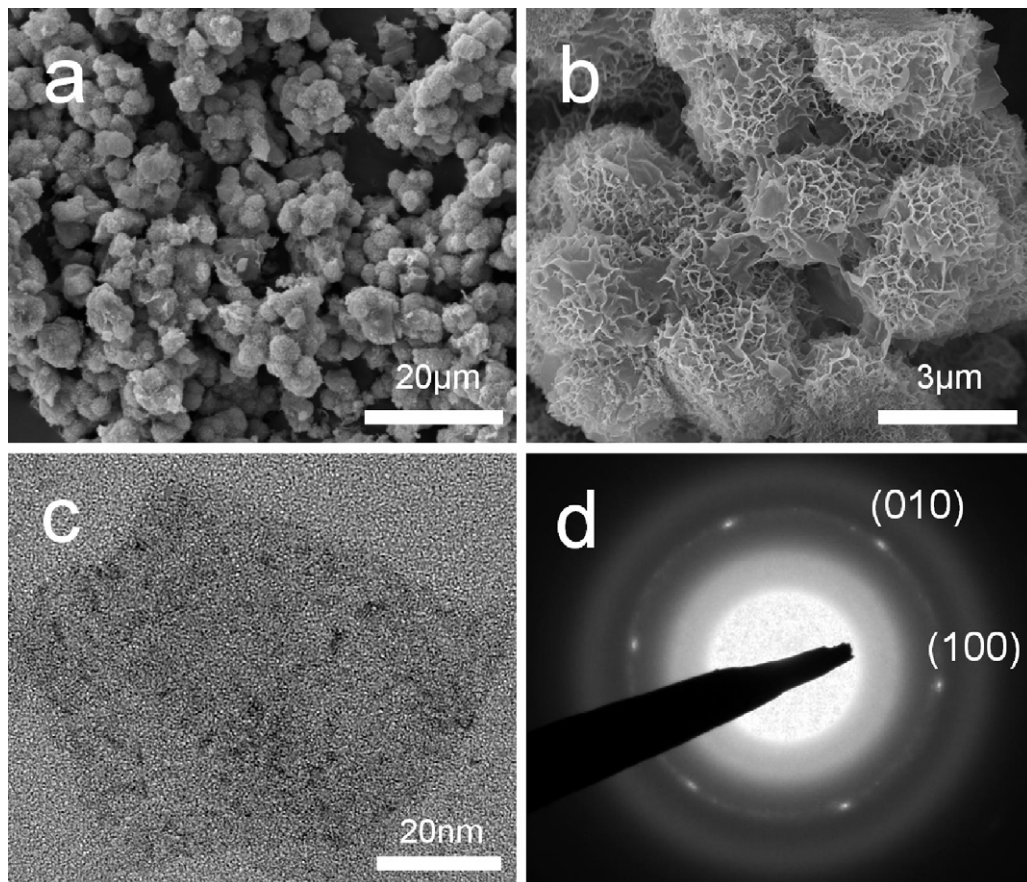


Fig. 5. TEM and SEM images of  $\alpha$ -Ni(OH)<sub>2</sub>: (a) and (b) SEM images  $\alpha$ -Ni(OH)<sub>2</sub> at different magnifications, (c) TEM image of nanosheet of  $\alpha$ -Ni(OH)<sub>2</sub>, and (d) SAED pattern taken from a nanosheet of  $\alpha$ -Ni(OH)<sub>2</sub>.

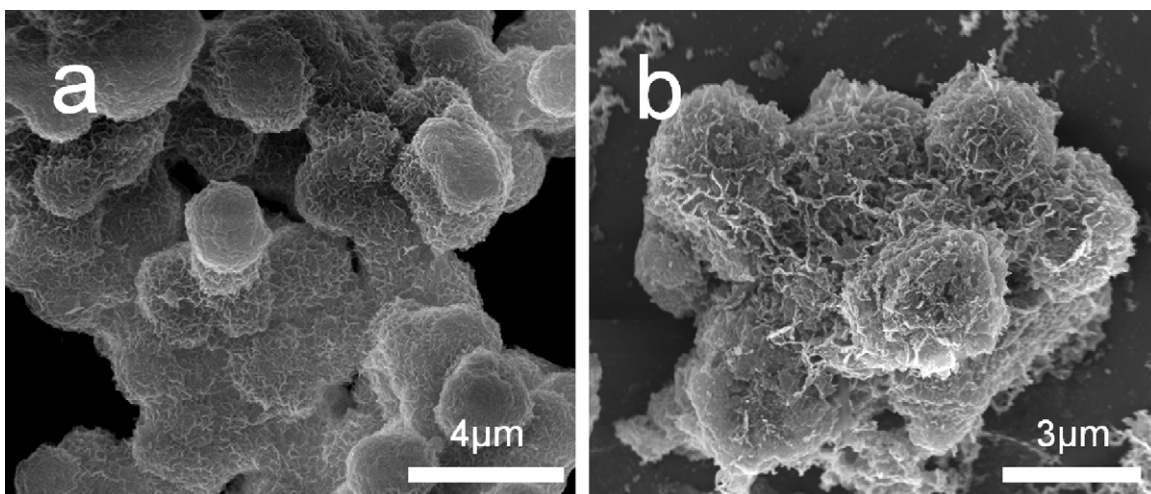


Fig. 6. SEM images of  $\alpha$ -Ni(OH)<sub>2</sub> obtained after reaching refluxing temperature for (a) 5 min and (b) 30 min.

area of hierarchical structures between active materials and electrolyte, consequently resulted in the high specific capacitance (vide post).

Thus far, in accordance with the employed route of synthesis, i.e., use of a template, alkaline source species, and synthetic methods, hexagonal plate [35], nanoribbon [36], hollow-type [37], fibrous-type [38], and flower-type [39]  $\alpha$ -Ni(OH)<sub>2</sub> have been reported. It is thought that unique morphologies such as these fabricated  $\alpha$ -Ni(OH)<sub>2</sub> microstructures could be synthesized with the aid of HMT. HMT has been used as a hydrolysis agent in the preparation of  $\alpha$ -Ni(OH)<sub>2</sub> [34,35]. The following reaction might occur in solution [40]:



Thus, in our synthetic procedure, the slow and progressive hydrolysis of only HMT lends the solution a basic condition and induces homogeneous precipitation of porous  $\alpha$ -Ni(OH)<sub>2</sub> microstructures. In addition, nickel sulfate was replaced with nickel nitrate, nickel acetate, and nickel chloride, respectively, but porous  $\alpha$ -Ni(OH)<sub>2</sub> microstructures could not be obtained. Sulfate anions are thought to affect the formation of porous morphologies, but further study is needed.

### 3.4. Electrochemical properties

The electrochemical properties and specific capacitance of the NiO microstructures were determined by cyclic voltammetry (CV) to evaluate their potential utility in supercapacitor applications. Fig. 9 shows the CV curves of N300, N400, and N500 at 20 mV s<sup>-1</sup>, respectively. Two strong current peaks were observed, indicating that the capacitance of NiO mainly resulted from pseudocapacitive capacitance based on a fast redox mechanism. Two strong current peaks correspond to a redox reaction according to the following equation.



The anodic peak at roughly 0.31 V is related to the oxidation of NiO to NiOOH, and the cathodic peak at about 0.21 V is due to its reverse process similar to previous reports. Therefore, the two strong redox reaction peaks in the CV curves are responsible for the pseudocapacitance of the NiO microstructures. As increased the calcinations temperature, both cathodic and anodic current density under CV curves decreased. As redox reaction occurs at the interface of electrolyte and NiO particles, high specific capacitance can be obtained under condition of high specific surface area of active materials and narrow pore distribution with many channels for diffusion of OH<sup>-</sup> ions. Therefore, specific capacitance of N300 is

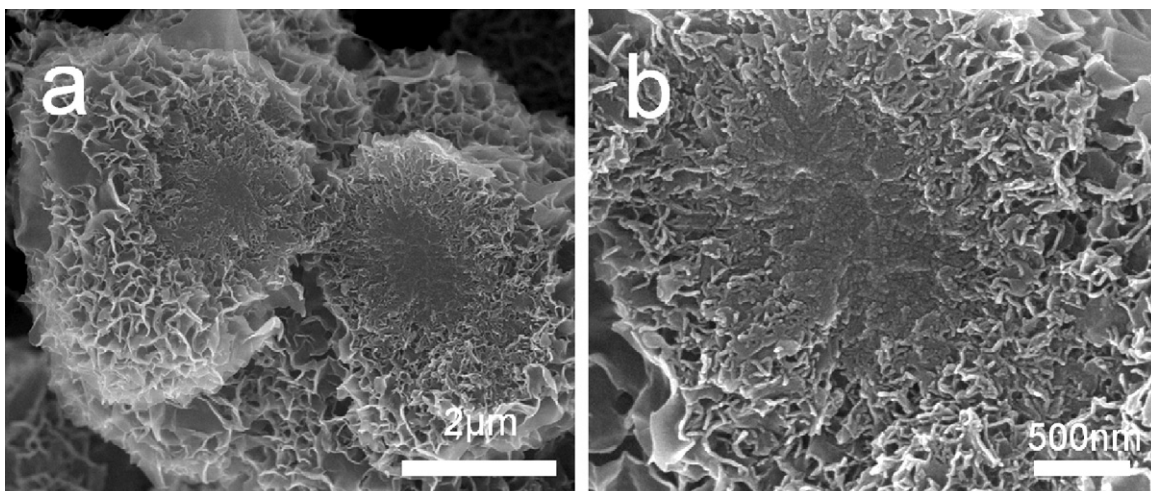


Fig. 7. SEM images of broken  $\alpha$ -Ni(OH)<sub>2</sub> at different magnifications.

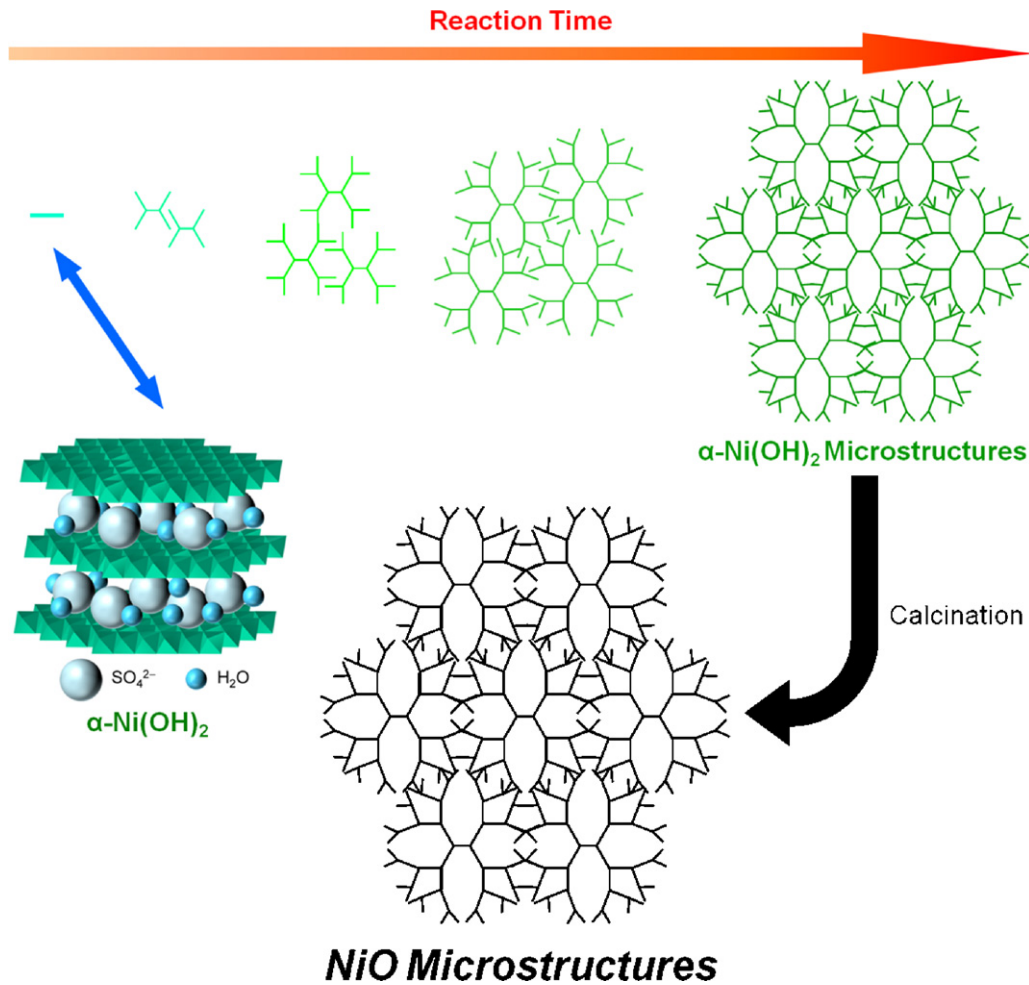


Fig. 8. Proposed growth mechanism for  $\alpha$ -Ni(OH)<sub>2</sub> microstructures.

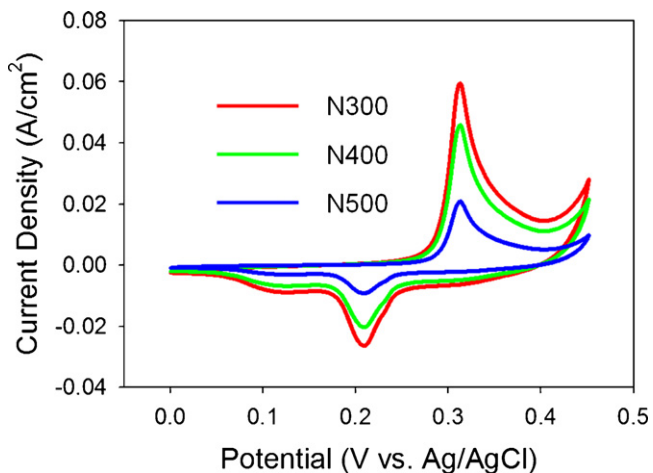


Fig. 9. Cyclic voltammetry curves of N300, N400, and N500.

highest among prepared samples. This observation is in agreement with the results reported earlier [11,12,14].

Fig. 10a shows the decay in specific capacitance as a function of the scan rate. Specific capacitance at 2, 5, 10, and 20  $\text{mV s}^{-1}$  scan rate is 718, 470, 420, and 403  $\text{F g}^{-1}$ , respectively, which is shown in Fig. 10b. Calculated parameter,  $q_a$ ,  $q_c$ , and specific capacitance of N300 at different scan rates are tabulated in Table 2. As the scan rate increased, the potential of the anodic and cathodic peaks shifted

in more positive and negative directions, due to the limitation of the ion diffusion rate to satisfy electronic neutralization during the redox reaction.

Since long cycle-life is in the most important criterion for a supercapacitor, an endurance test of NiO microstructures was conducted using CV 1000 times between 0.0 and 0.45 V at a nominal scan rate of 20  $\text{mV s}^{-1}$ . The CV curves and the specific capacitances as a function of cycle number are plotted in Fig. 11a and b. All the CV curves almost overlapped with each other, indicating good cycling stability. The degradation of specific capacitance was about 5.2% after 1000 cycles. It is believed that the unique mesoporous NiO microstructures allow easy access of  $\text{OH}^-$  to the NiO electrode surface, and thereby offer high specific capacitance and less degradation during the cycle test.

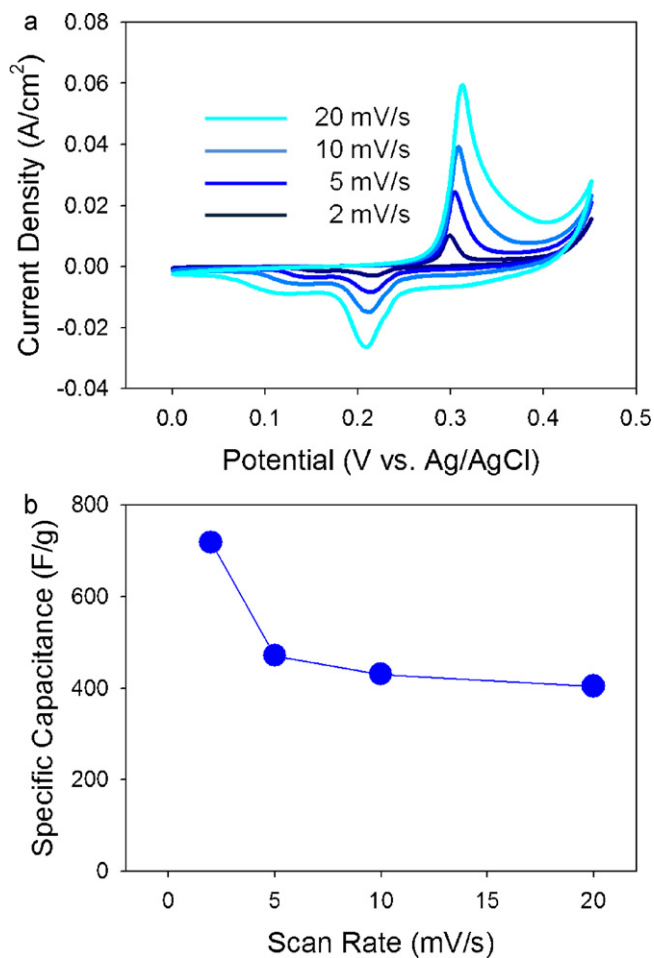
The detailed characteristics of a capacitive electrode can be observed by electrochemical impedance spectroscopy (EIS) analyzed using a Nyquist plot, which represents the imaginary part

Table 2

Calculated parameter,  $q_a$ ,  $q_c$ ,  $q_a + q_c$ , and specific capacitance of N300 at different scan rate.

Scan rate ( $\text{mV s}^{-1}$ )	$q_a$ (C)	$q_c$ (C)	$q_a + q_c$ (C)	$C$ ( $\text{F g}^{-1}$ ) <sup>a</sup>
2	0.3204	0.1965	0.5169	718
5	0.2041	0.1344	0.3385	470
10	0.1774	0.1255	0.3029	420
20	0.1654	0.1253	0.2907	403

<sup>a</sup> Specific capacitances were calculated by  $C = (q_a + q_c) / 2m\Delta V$ , where  $m$  ( $\text{g}$ ) = 0.0008,  $\Delta V$  (V) = 0.45.



**Fig. 10.** (a) Cyclic voltammograms of N300 at scan rate of 2, 5, 10, and 20  $\text{mV s}^{-1}$  and (b) specific capacitance as a function of scan rate of N300.

( $Z''$ ) and real part ( $Z'$ ) of impedance. Fig. 12 shows Nyquist plots of the capacitive electrode before and after 1000 cycles at an applied potential of 0.25 V (vs. Ag/AgCl). The impedance spectra are almost similar in shape, which consist of one semicircle at high frequency, and followed by a straight line at the low frequency range. Such a pattern can be fitted by an equivalent circuit for impedance analysis, and is shown in the upper right inset of Fig. 12a, where  $R_s$  is the solution resistance of the electrochemical system,  $C_{dl}$  is

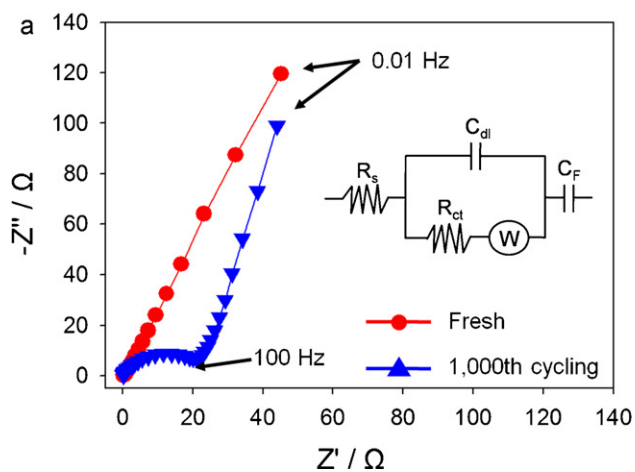


**Fig. 12.** Nyquist plots of N300 electrode before and after 1000 cycles at an applied potential of 0.25 V (vs. Ag/AgCl). The right inset (a) is the proposed equivalent circuit for the EIS spectrum and (b) indicates enlarged Nyquist plots in the high frequency region.

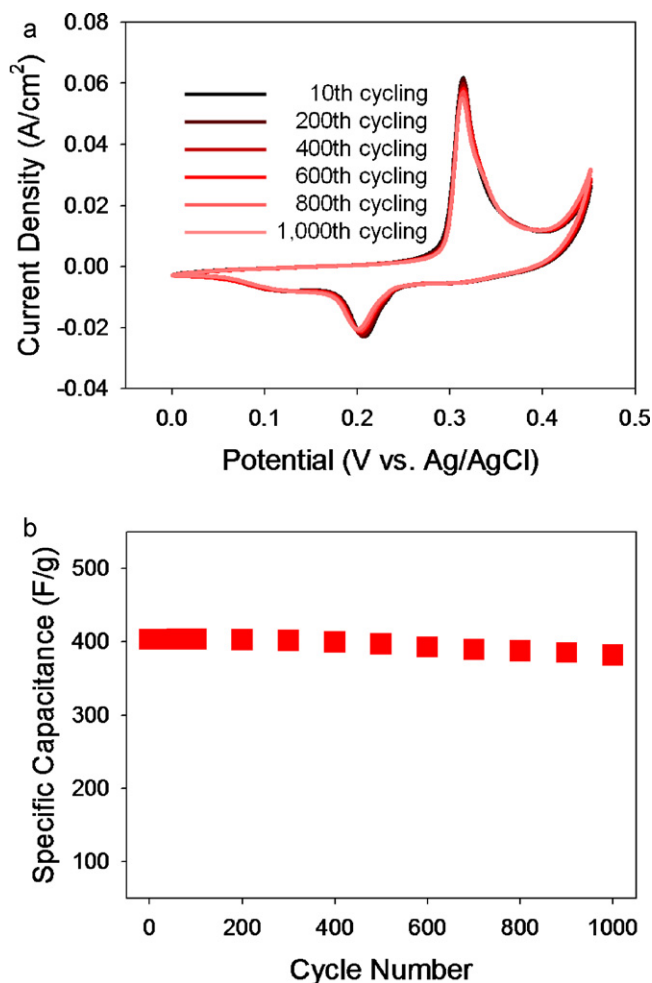
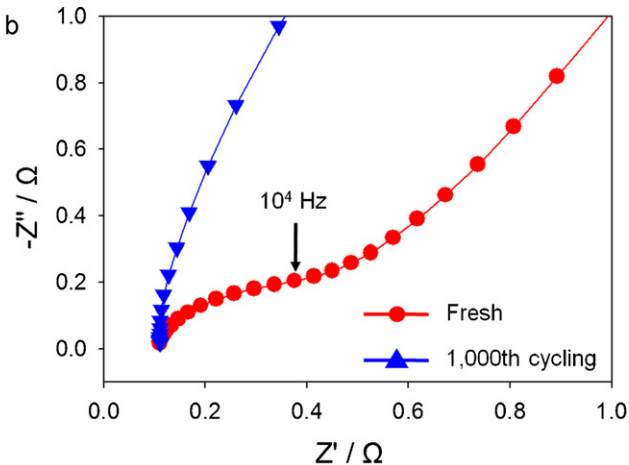


**Fig. 11.** Cycle test of N300: (a) cyclic voltammograms of 10 cycles to 1000 cycles at a 20  $\text{mV s}^{-1}$  scan rate and (b) variation in the specific capacitance as a function of the cycle number at a 20  $\text{mV s}^{-1}$  scan rate.

a double layer capacitor,  $C_F$  is a Faradaic pseudocapacitor,  $W$  is Warburg impedance, and  $R_{ct}$  is Faradaic interfacial charge transfer resistance. The solution resistance  $R_s$  and the charge transfer resistance  $R_{ct}$  can be obtained from the Nyquist plot, where the high frequency semicircle intercepts the real axis at  $R_s$  and  $(R_s + R_{ct})$ , respectively. As shown in Fig. 12b, the solution resistance  $R_s$  are



almost same, namely,  $0.1 \Omega$ , for two electrodes. However, there is a major difference about the charge-transfer resistance ( $R_{ct}$ ). After 1000 cycles, the charge-transfer resistance for the capacitive electrode is increased. As the charge-transfer resistance ( $R_{ct}$ ) is normally resulting from ionic resistance of electrolyte, the intrinsic resistance of the active materials, and the contact resistance at the active material/current collector interface, increase in the charge-transfer resistance ( $R_{ct}$ ) is caused by the loss of adhesion of some active materials or composite crack with the current collector during the long term charge/discharge cycling.

#### 4. Conclusion

We have demonstrated a simple and template-free method for fabricating NiO microstructures.  $\alpha$ -Ni(OH)<sub>2</sub> microstructures were successfully synthesized by HMT hydrolysis. Subsequent calcination at 300 °C yielded NiO microstructures that retained the original morphologies of the  $\alpha$ -Ni(OH)<sub>2</sub>. The prepared NiO microstructures had large BET specific surface area, narrow pore size distribution, and high pore volume, for characteristics that are ideal for supercapacitor applications. The NiO microstructures produced high specific capacitance and showed good retention for more than 1000 cycles in a cycling test. This article is the first report about synthesis of NiO electrode by HMT hydrolysis. We expect to obtain NiO with unique morphologies by other method using HMT, which could result in superior candidates for supercapacitor applications.

#### Acknowledgments

This work was supported by the BK 21 Program and Basic Science Research Program through the National Research Foundation of Korea (NRF) funded by the Ministry of Education, Science and Technology (2009-0076882).

#### References

- [1] M. Winter, R.J. Brodd, Chem. Rev. 104 (2004) 4245.
- [2] L.L. Zhang, X.S. Zhao, Chem. Soc. Rev. 38 (2009) 2520.

- [3] H.K. Jeong, M. Jin, E.J. Ra, K.Y. Sheem, G.H. Han, S. Arepalli, Y.H. Lee, ACS Nano 4 (2010) 1162.
- [4] T.E. Rufford, D. Hulicova-Jurcakova, Z. Zhu, G.Q. Lu, J. Phys. Chem. C 113 (2009) 19335.
- [5] S. Chen, J. Zhu, Q. Han, Z. Zheng, Y. Yang, X. Wang, Cryst. Growth Des. 9 (2009) 4356.
- [6] K. Wang, J. Huang, J. Wei, J. Phys. Chem. C 114 (2010) 8062.
- [7] C.C. Hu, K.H. Chang, M.C. Lin, Y.T. Wu, Nano Lett. 6 (2006) 2690.
- [8] R.R. Bi, X.L. Wu, F.F. Cao, L.Y. Jiang, Y.G. Guo, L.J. Wan, J. Phys. Chem. C 114 (2010) 2448.
- [9] K.H. Chang, C.C. Hu, C.Y. Chou, Chem. Mater. 19 (2007) 2112.
- [10] J. Zhang, J. Ma, L.L. Zhang, P. Guo, J. Jiang, X.S. Zhao, J. Phys. Chem. C 114 (2010) 13608.
- [11] C. Yu, L. Zhang, J. Shi, J. Zhao, J. Gao, D. Yan, Adv. Funct. Mater. 18 (2008) 1544.
- [12] Y.G. Wang, Y.Y. Xia, Electrochim. Acta 51 (2006) 3223.
- [13] P. Justin, S.K. Meher, G.R. Rao, J. Phys. Chem. C 114 (2010) 5203.
- [14] W. Xing, F. Li, Z.F. Yan, G.Q. Lu, J. Power Sources 134 (2004) 324.
- [15] C. Yuan, X. Zhang, L. Su, B. Gao, L. Shen, J. Mater. Chem. 19 (2009) 5772.
- [16] T. Zhu, J.S. Chen, X.W. Lou, J. Mater. Chem. 20 (2010) 7015.
- [17] H.S. Nam, J.S. Kwon, K.M. Kim, J.M. Ko, J.D. Kim, Electrochim. Acta 55 (2010) 7443.
- [18] J. Yan, E. Khoo, A. Sumboja, P.S. Lee, ACS Nano 4 (2010) 4247.
- [19] X. Du, C. Wang, M. Chen, Y. Jiao, J. Wang, J. Phys. Chem. C 113 (2009) 2643.
- [20] T. Nathan, A. Aziz, A.F. Noor, S.R.S. Prabaharan, J. Solid State Electrochem. 12 (2008) 1003.
- [21] M.S. Wu, C.H. Yang, M.J. Wang, Electrochim. Acta 54 (2008) 155.
- [22] K.R. Prasad, N. Miura, Appl. Phys. Lett. 85 (2004) 4199.
- [23] M. Wu, J. Gao, S. Zhang, A. Chen, J. Power Sources 159 (2006) 365.
- [24] U.M. Patil, R.R. Salunkhe, K.V. Gurav, C.D. Lokhande, Appl. Surf. Sci. 255 (2008) 2603.
- [25] Y.Z. Zheng, H.Y. Ding, M.L. Zhang, Mater. Res. Bull. 44 (2009) 403.
- [26] J.W. Lang, L.B. Kong, W.J. Wu, Y.C. Luo, L. Kang, Chem. Commun. 44 (2008) 4213.
- [27] J.Y. Lee, K. Liang, K.H. An, Y.H. Lee, Synth. Met. 150 (2005) 153.
- [28] F.B. Zhang, Y.K. Zhou, H.L. Li, Mater. Chem. Phys. 83 (2004) 260.
- [29] C. Yuan, X. Zhang, Q. Wu, B. Gao, Solid State Ionics 177 (2006) 1237.
- [30] Y.Z. Zheng, M.L. Zhang, Mater. Lett. 61 (2007) 3967.
- [31] H. Pang, Q. Lu, Y. Zhang, Y. Li, F. Gao, Nanoscale 2 (2010) 920.
- [32] B.J. Lee, S.R. Sivakkumar, J.M. Ko, J.H. Kim, S.M. Jo, D.Y. Kim, J. Power Sources 168 (2007) 546.
- [33] R.Y. Song, J.H. Park, S.R. Sivakkumar, S.H. Kim, J.M. Ko, D.Y. Park, S.M. Jo, D.Y. Kim, J. Power Sources 166 (2007) 297.
- [34] M.Y. Cheng, B.J. Hwang, J. Colloid Interf. Sci. 337 (2009) 265.
- [35] S. Ida, D. Shiga, M. Koinuma, Y. Matsumoto, J. Am. Chem. Soc. 130 (2008) 14038.
- [36] D. Yang, R. Wang, M. He, J. Zhang, Z. Liu, J. Phys. Chem. B 109 (2005) 7654.
- [37] X. Song, L. Gao, J. Phys. Chem. C 112 (2008) 15299.
- [38] P. Jeevanandam, Y. Koltypin, A. Gedanken, Nano. Lett. 1 (2001) 253.
- [39] L. Xu, Y.S. Ding, C.H. Chen, L. Zhao, C. Rimkus, R. Joesten, S.L. Suib, Chem. Mater. 20 (2008) 308.
- [40] Y.W. Chen, Q. Qiao, Y.C. Liu, G.L. Yang, J. Phys. Chem. C 113 (2009) 7497.